ARTICLE OPEN

Check for updates

Metallurgical pathways of lead leaching from brass

Te Zhu[1], Wei Li[1], Jonathan Chun Ming Kwok[1], Kai Wing Siu[1], Lu Yin[1] and Alfonso Hing Wan Ngan[1]✉

Leaded (Pb) brass components used in water pipeworks are prone to lead leaching following soldering or brazing during installation. Synchrotron radiation X-ray imaging shows that in the initial state of potable-water grade brass samples, Pb exists mainly as isolated or linked-together particles from sub-micron to several microns large. On heating to the usual soldering temperature of ~200 °C, the Pb contents surface rapidly via diffusion pathways involving an interpenetrating Pb–brass structure with orientation relationship $(11\bar{1})_{\alpha\text{-brass}}//(220)_{Pb}$; $[011]_{\alpha\text{-brass}}//[\bar{1}13]_{Pb}$. On heating to the usual brazing temperature of 700 °C, the Pb particles melt and expand in volume, with the Pb content forced into the brass lattice preferentially along $\{101\}_{\alpha\text{-brass}}$ planes, forming Pb phase of low sphericity or even large sheets. On immersion in water, the surfaced Pb particles are oxidized to form PbO needles along the normal direction of $\{\bar{2}\bar{2}2\}_{PbO}$ planes, which are then easily washed away to cause Pb leaching.

npj Materials Degradation (2023)7:69 ; https://doi.org/10.1038/s41529-023-00389-8

INTRODUCTION

Lead (Pb) is a prevalent heavy metal that is regulated by environmental protection agencies because it pollutes the environment[1–4] and can have harmful health effects such as neurological damage and adverse pregnancy outcomes if consumed[5,6]. The current Pb guideline, last revised in 1993, stipulates a maximum acceptable concentration of 10 µg/L, based on the World Health Organization's provisional tolerable weekly intake level below which no increase in blood lead levels and therefore no anticipated increase in health risks should happen. Poisoning caused by excessive lead in drinking water still occurs today, primarily due to the leaching of lead from components used in distribution and plumbing systems. As a result, regulations and engineering standards have been developed by jurisdictions for lead in components used in drinking-water piping systems. For instance, the British Standards specify that copper alloy fittings for potable water use should contain no more than 4–6 wt% Pb for valves and 0.5–2.5 wt% Pb for taps[7]. Meanwhile, according to US standards, the wetted surfaces of nominally lead-free copper alloys for potable water use are still permitted to contain Pb up to 0.25 wt%[8].

The so-called lead-free grade of brass for potable-water applications (referred to as pw-brass hereafter) bounds to contain Pb[9]. From time to time, Pb leaching into drinking water is reported worldwide[10–18], and one possible reason is due to the Pb contents in pw-brass pipelines and components, especially in newly installed conditions[19]. Traditionally, Pb is added into pw-brass to ease machining, and given the long history of using brass to make potable-water components and the vast amounts of brass pipelines and components already installed, no jurisdiction has announced any plan or timetable to ban the use of pw-brass in pipeworks. Interestingly, despite the importance of the problem, only the Pb-enhanced machinability of brass due to Pb surfacing was studied briefly in the 1970s[20], and an understanding of the metallurgical pathways of the Pb leaching process from pw-brass has remained non-existent. In particular, given that brass and Pb have no mutual solubility limit in the phase diagram[21], it is not known in what forms Pb would exist inside pw-brass, and how Pb would migrate to the specimen surface to cause leaching into contacting water.

Recent experiments[19] have shown that pre-heat treatment of pw-brass can result in accelerated Pb leaching. In these experiments, pre-heat treatments at either 200 or 700 °C were carried out before the Pb-leaching tests to simulate the soldering (200 °C) or brazing (700 °C) joining process for pipe-work installation. At 200 °C the Pb content in pw-brass is still in the solid state, while at 700 °C the Pb should be molten, but at the final Pb-leaching conditions in immersion tests, the Pb should be in solid state[22]. A detailed explanation of why pre-heat treatment accelerates Pb-leaching would require detailed knowledge of the Pb distribution in the initial brass as well as that after the pre-treatment. For instance, in Fig. 1 from the present work (details explained later), the 700 °C pre-treated state leaches at about the same rate as the 200 °C state for heating times shorter than around 20 mins, but the leaching rate accelerates significantly after 20 mins, which possibly indicates a non-uniform distribution of the Pb content inside the brass. Therefore, it is not the scope of the present paper to discuss how the pre-treatment duration would quantitatively affect the lead-leaching rate—such a study would require systematic control of the initial Pb distribution in brass samples which would be a formidable task given the high metastability or instability of the Pb segregation inside brass due to the mutual immiscibility of the two phases.

Instead, in this paper, our objective is to understand the metallurgical pathways for Pb leaching in a general context, based on the premise that no matter whether or how a pw-brass sample is pre-heat treated, there can only be two possible forms of Pb content, namely, (i) that in a connected mesh or network form that extends from the surface to the sample's interior, and (ii) isolated Pb particles embedded in the brass matrix. The present work embodies our latest discoveries on the metallurgical pathways of lead diffusion, surfacing, and leaching into contacting water. The immiscible nature of Pb in brass gives rise to elusive, free forms of Pb as isolated particles or connected segregations along the brass grain boundaries or at their triple points. Upon heating under common conditions akin to soldering or brazing operations during pipework installation, these free forms of Pb adopt fascinating pathways for diffusion, surface interaction, and leaching, including forming an unseen before interpenetrating lattice with the brass matrix, thin sheets within the brass, popping up as free particles

[1]Department of Mechanical Engineering, University of Hong Kong, Pokfulam Road, Hong Kong, China. ✉email: hwngan@hku.hk

on the specimen surface and oxidizing into lead-oxide needles when immersed into water. In the below, these microstructures are characterized using techniques such as synchrotron radiation X-ray imaging, FIB-sectioning, and HRTEM, and then rationalized through molecular dynamics simulations. These results represent not only interesting microstructure evolution unseen before in an immiscible alloy system but also a major step towards a mechanistic understanding of the important problem of lead leaching.

RESULTS

Figure 2 shows the specific morphologies of two forms of Pb mentioned above in a pw-brass. Here, a pw-brass sample surface was etched for 30 s in phosphoric acid, which preferentially etched away the brass phase but not the Pb contents inside. The SEM micrograph in Fig. 2b shows the two forms of Pb contents protruded from the etched brass surface: (i) Pb segregated along grain boundaries (GBs), and (ii) micron-sized isolated Pb particles within brass grains. For GB-segregated Pb, Fig. 2b shows that many of the GBs are decorated with sub-micron thick Pb layers of lighter contrast, and at the same time, many big Pb particles (a few to ~10 microns large) also of a similar lighter contrast are seen situated at the GBs, especially at their triple junctions, and so they are of the category (i) above. On the other hand, there are also isolated Pb particles smaller than 1 micron within the brass grains, which are of the category (ii). Figure 2c schematically shows the preferential etching and the exposure of the two types of Pb contents on the etched surface. The objective of this paper is to discuss how these two forms of Pb content can leach out from pw-brass.

Previous work has revealed that heat treatment will increase the Pb content on the pw-brass surface[19], and this has important repercussions on Pb leaching because pipework installation often involves joining pw-brass components by soldering or brazing. Brass soldering and brazing typically involve heating up to ~200 and ~700 °C, respectively, for a few minutes. Therefore, below, the Pb distribution in pw-brass after such treatments is first presented, followed by the surfacing of Pb during the treatments.

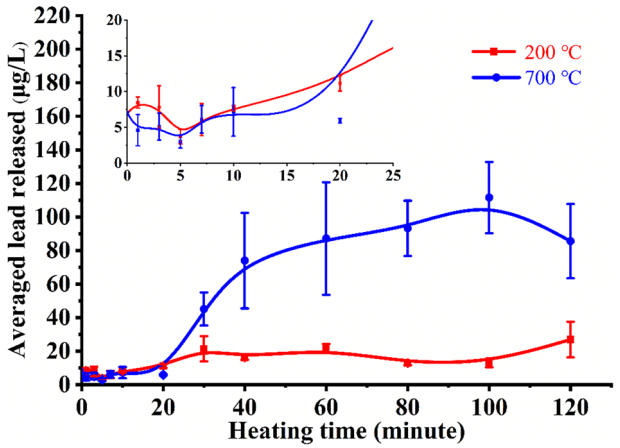

Fig. 1 Pb leaching results. Results of Pb leaching tests by immersion in 50 ml of tap water for 24 h, after heating at 200 and 700 °C for different durations.

Pb distribution in potable-water grade brass (pw-brass) after heat pre-treatment

The size and sphericity of Pb contents within pw-brass after 200 and 700 °C treatment for 5 min were analyzed by synchrotron radiation X-ray imaging and the results are shown in Fig. 3. After heating up to 200 °C for 5 min, Fig. 3a, d, and g show that the Pb exists mainly in the form of isolated or linked together particles (some at triple points of brass grain boundaries) of sphericity higher than ~0.4, and sizes from sub-micron to several microns. Figure 4a–c shows the morphology and element maps of a Pb particle at a triple point of brass grains observed by TEM. The Pb element map in Fig. 4c shows that the boundary of the Pb particle is enriched with Pb, but Pb also spreads to the surrounding brass matrix. It can be seen from Fig. 4a that the triple-point particle actually has a nanocrystalline structure, which, interestingly, extends into the surrounding brass matrix over a depth of around 250 nm which is also the depth of Pb penetration as seen from Fig. 4c. The HRTEM image in Fig. 4d shows that this region of Pb-penetrated brass contains nanocrystals of around 15 nm in

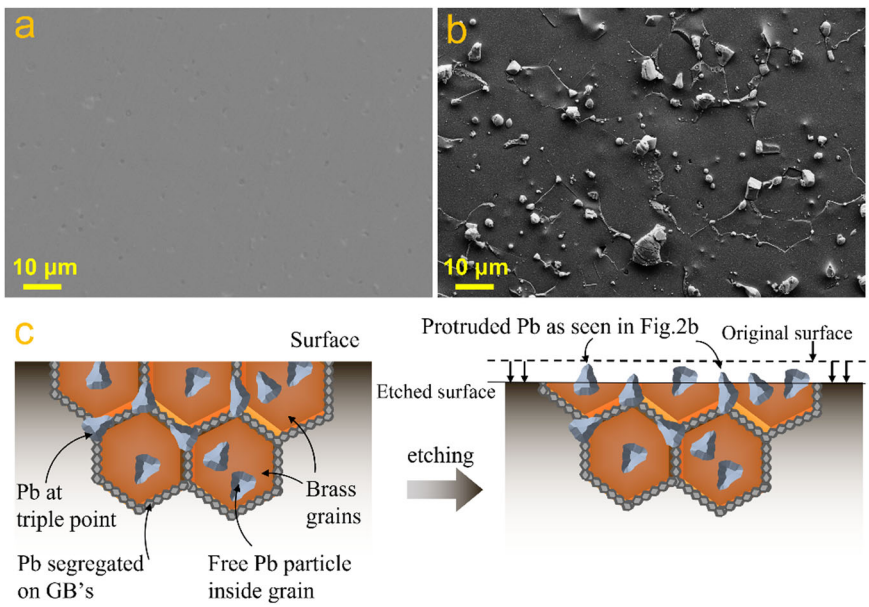

Fig. 2 The specific morphologies of two forms of Pb in a pw-brass. a SEM of pw-brass surface before etching. **b** SEM of pw-brass surface etched by phosphoric acid in 30 s. **c** Schematic showing two forms of Pb content of isolated particles and GB segregation forming a connected network.

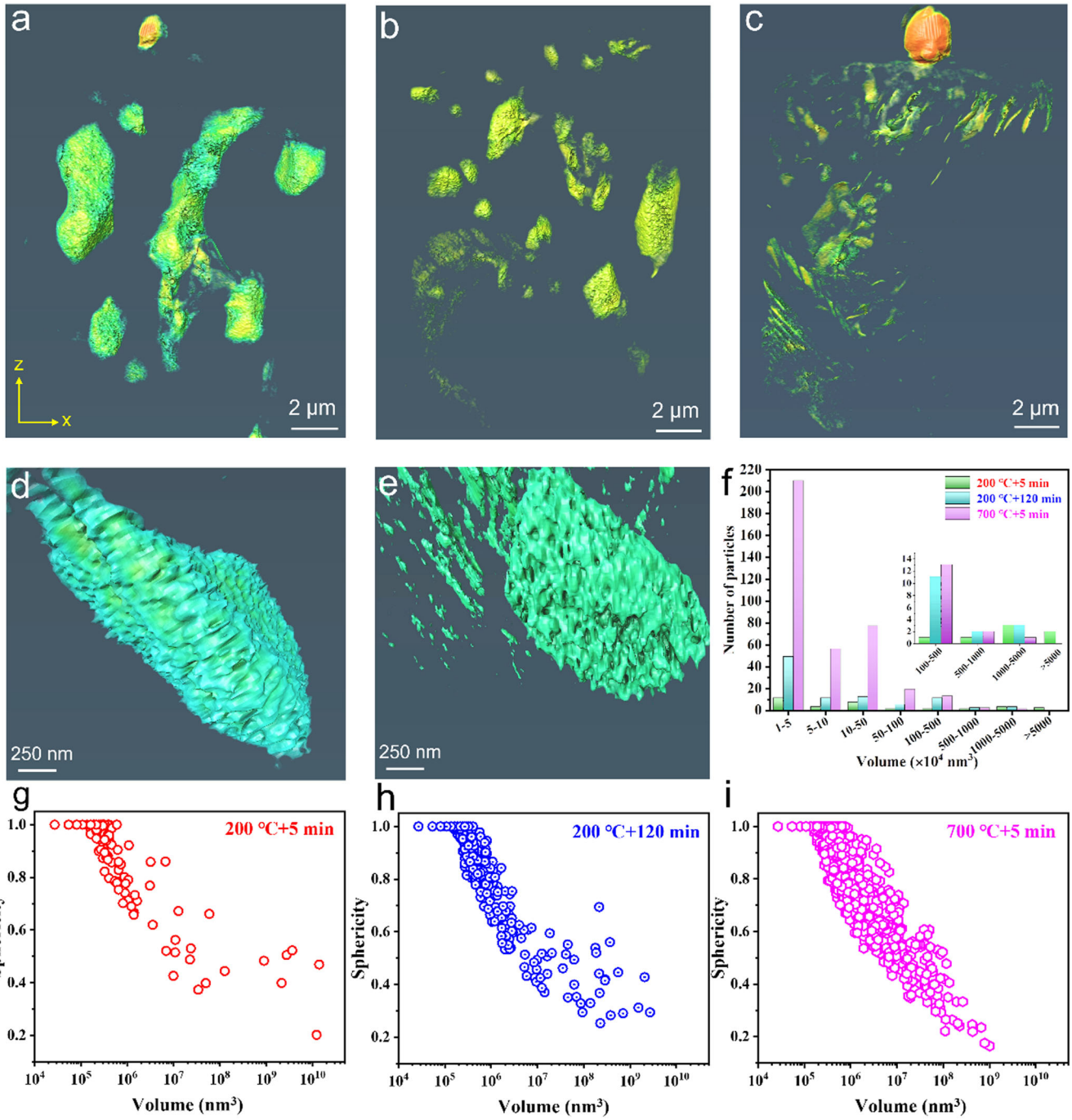

Fig. 3 Results of synchrotron radiation X-ray imaging. a Sample heated at 200 °C for 5 min (hide brass to see the 3D distribution of Pb). **b** Sample heated at 200 °C for 120 min. **c** Sample heated at 700 °C for 5 min. **d** High magnification of the picture for the sample heated at 200 °C for 5 min. **e** High magnification of the picture for the sample heated at 700 °C for 5 min. **f** Size distribution of lead particles. **g**–**i** Shape distribution of lead particles (the extent to which different sizes of lead particles are close to spherical shape).

diameter of similar orientation, separated by wide grain boundaries of around 2 nm in width. Nano-twins are seen in some of the nanocrystals, such as the one marked by the blue frame in Fig. 4d, the twin relationship of which is indicated clearly by the fast Fourier transform (FFT) of the HRTEM image in Fig. 4f. In other brass nanocrystals, such as the one marked by the red frame in Fig. 4d, coarse lattice fringes of Pb are seen superimposing on the fine lattice fringes of α-brass as shown by the FFT in Fig. 4e. This interesting result indicates that the heat treatment at 200 °C causes Pb from the initial triple-point particle to penetrate into the surrounding α-brass lattice, forming a $[011]_{\alpha\text{-brass}}//[\bar{1}13]_{Pb}$, $(11\bar{1})_{\alpha\text{-brass}}//(220)_{Pb}$ orientation relationship as shown in Fig. 4e. Figure 4g shows the process schematically. At 200 °C, corresponding to ~0.8 of the absolute melting temperature of Pb, Pb atoms in an original dense Pb phase (i.e. the triple-point particle in Fig. 4a) quickly diffuse into the nearby α-brass. At such a high homologous temperature, lattice diffusion should overtake grain-boundary diffusion, so that a major fraction of the Pb flux diffuses into the lattice of α-brass, instead of along the limited pathway of the three-grain boundaries connected to the triple-point particle. Pb atoms thus quickly enter into the α-brass lattice, but are nevertheless unstable if they are to distribute uniformly

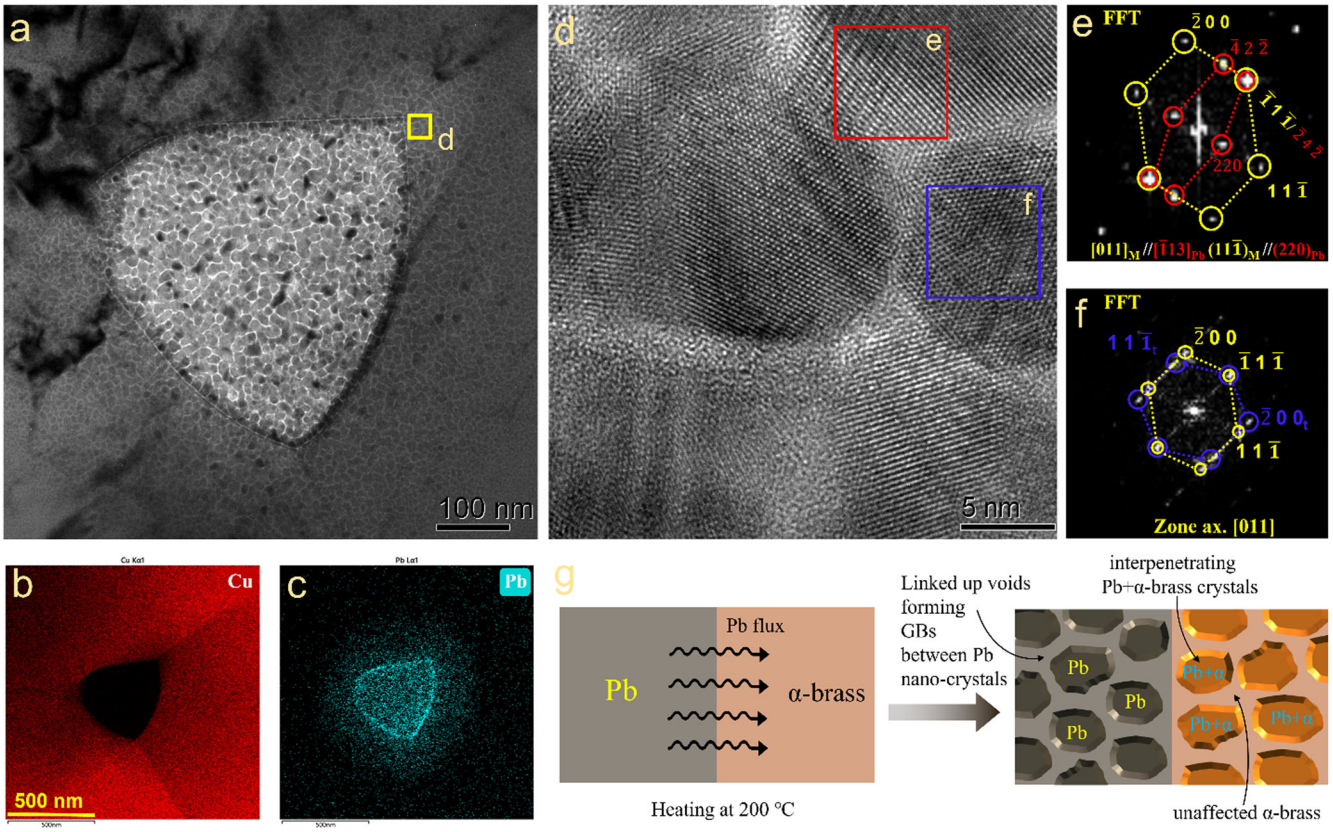

Fig. 4 TEM analysis of a Pb particle at triple point of brass grains in a sample heated to 200 °C for 5 min. a TEM bright-field image of the particle and its surrounding. **b**, **c** Element maps. **d** HRTEM image of the brass matrix in the frame marked in (**a**). **e**, **f** FFT of the HRTEM image in the corresponding frames in (**d**). **g** Schematic showing the formation of the observed microstructure.

with the brass matrix since the two phases have no solubility limit for one another. Hence, over a short time, the Pb atoms segregate into nano-domains with the abovementioned interpenetrating Pb + α-brass lattice structure, which is separated by Pb-depleted brass. Due to the presence of Pb, the Pb + α-brass nano-crystals exhibit darker contrast (Z-contrast) in the TEM compared with the Pb-depleted brass matrix, as shown in Fig. 4a, and the Pb also gives rise to the blue signal spikes in Fig. 4c in the brass surrounding the triple-point particle. For the original Pb triple-point particle, after a large quantity of Pb atoms has diffused away, the remaining particle now consists of nanocrystals separated by wide grain boundaries which are actually linked up voids with a bright contrast in the bright-field TEM, forming the maze-like structure in Fig. 4a. It is believed that this microstructure comprising nano-grains of interpenetrating lattices of Pb and α-brass in the brass matrix and Pb nanocrystals in the Pb phase is metastable, and given time, the Pb content in the brass may further re-organize by diffusion into nearby sinks such as grain boundaries, and the voided grain boundaries in the Pb particle may condense into large voids of high sphericity.

As for the Pb microstructure after heating at 700 °C for 5 min, Fig. 3i shows that the sphericity of the Pb content exhibits a remarkable drop to below ~0.4 for volumes larger than ~10^7 nm^3, compared with Fig. 3g and h for heat treatment at the lower temperature of 200 °C. Figure 5 shows different rotated views of the Pb content (green contrast) after heat treatment 700 °C for 5 min. In addition to 3D structures, Pb also exists in the brass matrix in sheet-like structures, which tally well with the reduced sphericity in Fig. 3i for large volumes. The emergence of the sheet structures of Pb after heat treatment at the higher temperature suggests that the Pb expands on melting and forces its way along specific crystallographic planes of the α-brass phase. To determine such crystal planes of α-brass, a sample heated at 700 °C for 5 min was cut using FIB and then subjected to ion imaging. Figure 6ai shows a case where the FIB cutting exposed a large area of a Pb sheet which is in dark contrast under ion imaging (straight spikes along another crystallographic direction, as well as two micron-sized Pb particles marked 1 and 2, are also seen attached to this large sheet). To determine the crystallographic orientation of the brass matrix behind the large Pb sheet, the sheet was gradually milled away by FIB as shown in Fig. 6a, b, which shows that, although the original appearance could not be maintained because of the serial ion milling, the two particles 1 and 2 are still visible which would serve as markers for the area of interest. Then, after the Pb sheet has been milled away, as confirmed by element mapping as shown in Fig. 6c–e, EBSD was performed on the remaining brass matrix to determine its crystallographic orientation. As shown in Fig. 6f, the orientation was [101], indicating that the habit plane of brass along which the Pb had forced its way through during melting was a (101). Returning to Fig. 6ai, as indicated by the blue arrows, the spikes attached to the main Pb sheet along $(101)_{brass}$ were therefore evidently Pb sheets along the orthogonal $(10\bar{1})_{brass}$ planes, which would be in an edge-on view in Fig. 6ai, and hence the spike-like appearance.

Pb surfacing during heat treatment

To see the actual surfacing of Pb during heating in the air would be very difficult since any surfaced Pb content would oxidize quickly alongside the matrix brass surface, and if such a treated surface is not polished before examination in an SEM, the surfaced Pb morphology would not be seen clearly. On the other hand, polishing for SEM examination would remove the surfaced Pb. Because of these difficulties, we chose to visualize the Pb surfacing

during in situ heating in a vacuum condition in the SEM. Figure 7 shows such an experiment in which a pw-brass sample was heated inside the SEM at 50 °C increments from room temperature to 200 °C, followed by 25 °C increments between 200 and 300 °C, and holding each temperature for 5 min, followed by a decrease in temperature to 200 °C for 5 min. In the back-scattered image mode shown in Fig. 7a–o, the Pb contents are in white contrast, as confirmed by element mapping (Supplementary Material Fig. 1).

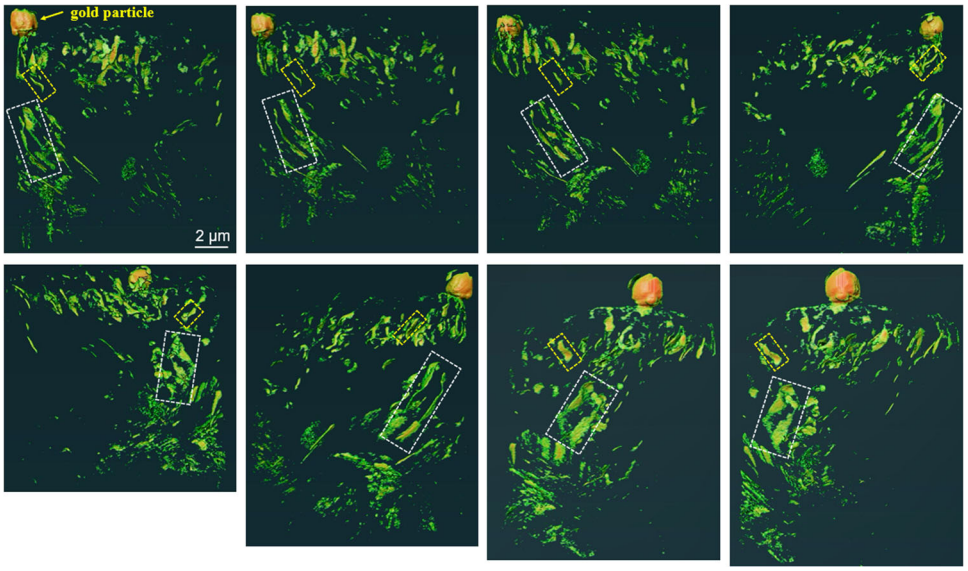

Fig. 5 Results of synchrotron radiation X-ray imaging (sample heated at 700 °C for 5 min). Pb is liquid at 700 °C. Each picture represents a different angle of view.

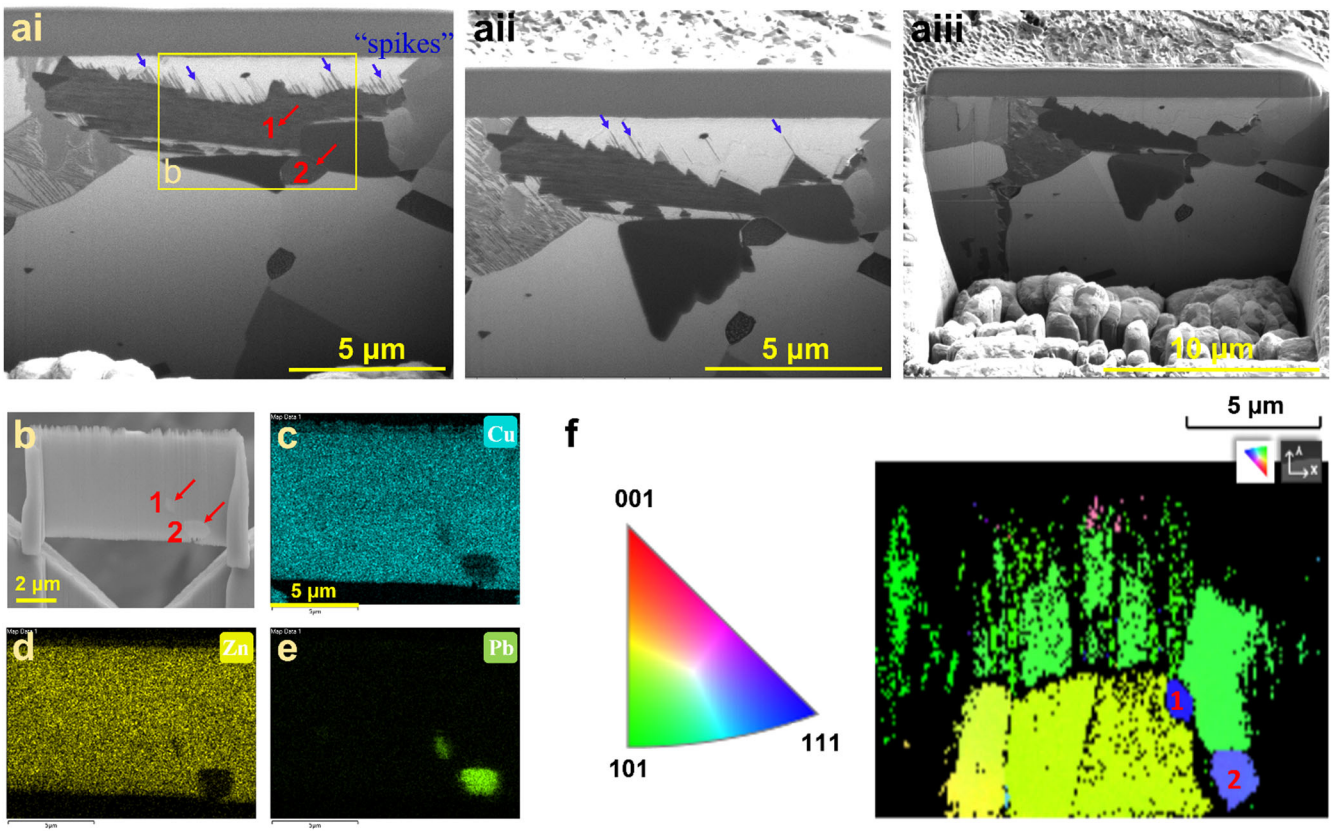

Fig. 6 Serial FIB milling of a pw-brass sample heated at 700 °C for 5 min. ai–aiii A ditch was first FIB milled to expose a cross-section perpendicular to the free surface of the sample. The cross-section containing a large Pb sheet was then subsequently milled and ion-imaged as shown in the three snapshots. **b**–**e** Electron image (**b**) and element maps (**c**–**e**) of the cross-section right after the large Pb sheet has been milled away. **f** EBSD of the brass matrix underlying the milled-away Pb sheet. In **a**, **b**, **f**, Pb particles 1 and 2 serve as markers for the area of interest.

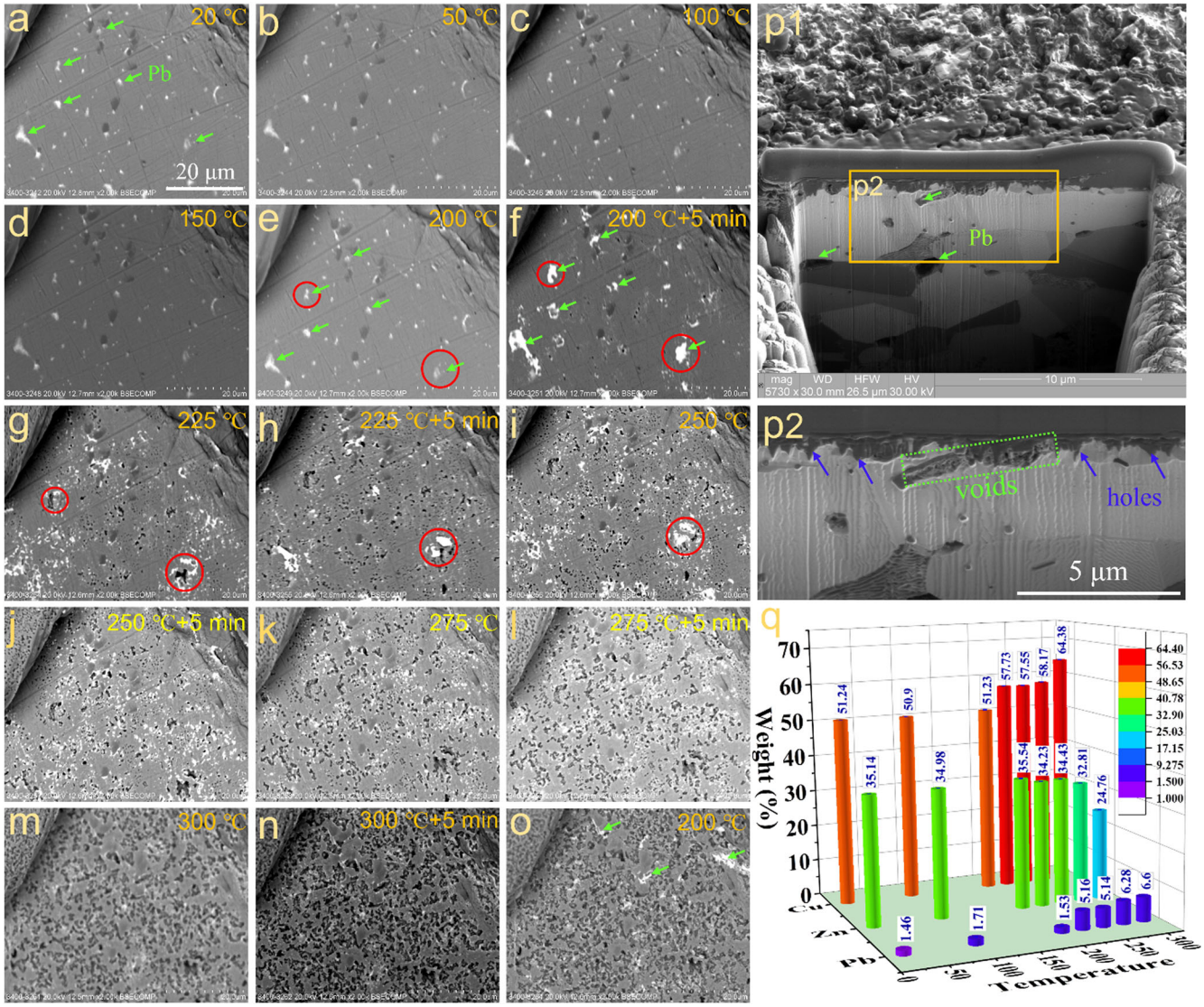

Fig. 7 Pb surfacing during in situ heating. The imaging was conducted by heating the brass samples at 50 °C increments from room temperature to 200 °C, followed by 25 °C increments between 200 and 300 °C, and holding each temperature for 5 min inside an SEM in a vacuum state, followed by a decrease in temperature to 200 °C for 5 min (**a**–**o**). The heated samples were then cut open with FIB (Fig. 7p1). Figure 7q shows the content of Pb on the heating surface detected by SEM-EDS.

No obvious change can be observed during in situ heating up to 200 °C (Fig. 7a–e), but after holding at 200 °C for 5 min (Fig. 7f), new Pb contents emerged and holes were developed on the surface. The emergence of new Pb contents and development of holes continued on further heating up to 250 °C (Fig. 7g–i), and on further heating beyond 250–300 °C (Fig. 7j–n) the surface became heavily pitted while EDAX measurement shows that the Pb content on the surface became stabilized (Fig. 7q). The stabilization of Pb content on the surface is likely caused by a balance between surfacing of Pb from the sample interior and the sublimation of surfaced Pb at the heated condition in a vacuum. Figure 7p1, p2 shows FIB cross-sections of the sample after the in situ heating cycle, revealing the presence of subsurface voids.

Diffusion voids left behind by Pb surfacing are frequently encountered in the present work as shown in Fig. 8. Figure 8a shows the FIB cross section of another pw-brass sample heated at 200 °C for 5 min, where voids are seen at a subsurface depth of around 1 micron in a large Pb phase close to the surface. Figure 8b shows a pw-brass surface heated at 200 °C for 5 min and then subjected to etching in phosphoric acid for 1 min to preferentially remove a thin surface layer of brass phase. Many voids of similar submicron sizes as the isolated Pb particles within the brass grains can be seen. In addition, the grain boundaries of the brass phase are decorated with Pb segregation (in light contrast), and large Pb particles are also seen to reside on triple points of the brass matrix. Figure 8c, d schematically shows the formation of voids from the larger Pb phase and isolated small Pb particles near the surface. The popping up of Pb contents from subsurface particles to the surface as illustrated by Fig. 8d happens very quickly in the temperature range of 200–300 °C. Figure 9 shows another experiment in which a pw-brass surface preferentially etched by phosphoric acid (Fig. 9a) was heated in situ inside the SEM at 290 °C. Here, the preferential acid etching allowed the initial Pb content to be seen more clearly by removing part of the surrounding brass matrix, and new Pb particles were seen popping up on the surface for just 1 min of heating (Fig. 9b).

Fate of surfaced Pb

Finally, it is of paramount importance to understand the fate of the surfaced Pb contents upon immersion into water. To this end,

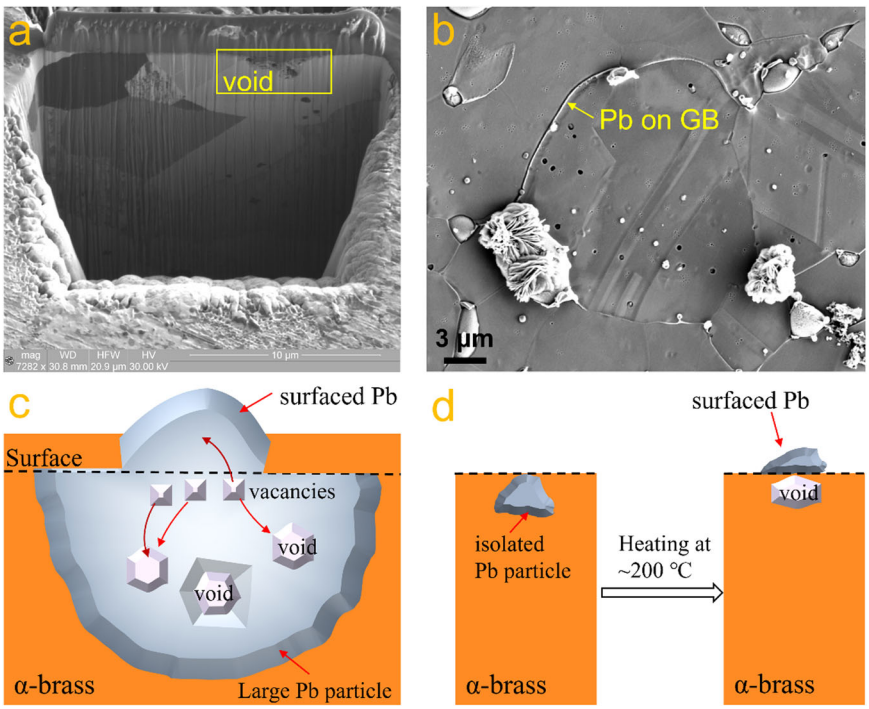

Fig. 8 Diffusion voids left behind by Pb surfacing. a FIB cross-section SEM of a pw-brass sample heated at 200 °C for 5 min, showing voids formed at sub-surface depth of around 1 micron inside a large Pb particle of a few microns in size. **b** Preferentially etched (by phosphoric acid for 1 min) pw-brass surface heated at 200 °C for 5 min, showing many voids of similar submicron sizes as the isolated Pb particles within brass grains. **c**, **d** Schematics of the Pb surfacing process from a large Pb phase (**c**) and a small Pb particle (**d**) near surface.

accelerated leaching tests were carried out on pw-brass with a standardized cylindrical-shell geometry of 22 mm inner diameter, 1.5 mm wall thickness, and 20 mm height. The samples were heated up in a furnace to 200 and 700 °C for durations of 1, 3, 5, 7, 10, 20, 30, 40, 60, 80, 100, and 120 min, then rested for 2 min to cool down and then tested for lead leaching by immersion in 50 ml of tap water at 75 °C for 24 h. Figure 1 shows the leaching results, indicating that after ~20 min of heating, the leaching rate of 700 °C pre-treated samples becomes significantly higher than that of the 200 °C pre-treated samples. Figure 10 shows the morphologies of Pb particles in samples subjected to the two heat treatments exposed by phosphoric-acid etching for 1 minute, before and after immersion in hot water at 75 °C. It is clear that in the exposed state (Fig. 10a1 and b1), the Pb particles are very solid and quite equiaxed in shape, but after 45 min of immersion in hot water (Fig. 10a2 and b2), the particles became loose 3D meshes of fine needles. EDAX and XRD measurements indicate that the needles are PbO (see Fig.10a3 and Supplementary Material Fig. 2). These loose needle-shaped particles have a much greater chance of being washed off the surface of the brass by running water than freshly exposed Pb particles, as confirmed by the three lead particles marked with red circles in Fig. 10a. It can be seen from Fig. 10b that the 700 °C case has a lot more Pb oxide formed, thus explaining the higher leaching rate in Fig. 1. For the case of immersion at ambient temperature, the Pb particle on the etched brass surface shown in Supplementary Material Fig. 3 after 60 min of immersion also has needle-shaped oxides formed.

The PbO needles were scraped from the sample surface and analyzed by TEM as shown in Fig. 11a–d. Most of these needles are less than 100 nm in diameter, and to facilitate the transmission of the electron beam, a needle with a diameter of ~40 nm as shown in Fig. 11a was selected to analyze its crystal structure. The selected area electron diffraction (SAED) result indicates that their growth (axial) direction is [$\bar{2}20.5938$] in the tetragonal crystal-structure system, which is the normal direction of the ($\bar{2}\bar{2}2$) plane (Fig. 11b).

DISCUSSION

The experimental results presented above unveil several interesting aspects of the Pb diffusion and leaching pathways in pw-brass:

1. On heating to 200 °C for a few minutes, Pb in the initial Pb particles diffuses into the brass matrix forming an unseen before interpenetrating structure with orientation relationship $(11\bar{1})_{\alpha\text{-brass}}//(220)_{Pb}$ and $[011]_{\alpha\text{-brass}}//[\bar{1}13]_{Pb}$, as shown in Fig. 4e. Pb diffusion also leads to the formation of voids of submicron sizes and at submicron sub-surface depths in the brass matrix (Fig. 8), and surfacing of submicron-sized Pb particles on the specimen (Fig. 9).
2. On heating to 700 °C for a few minutes, the Pb molten brass content grows into the brass matrix forming low-sphericity sheets preferentially along the $\{101\}_{\alpha\text{-brass}}$ planes (Fig. 6).
3. On immersion in water, the surfaced Pb contents on the 200 and 700 °C treated specimens quickly oxidize into long needles of PbO (Fig. 10).

In order to understand the brass/Pb orientation relationship after the 200 °C treatment in Fig. 4e, the interfacial and adhesion energy of the $(11\bar{1})_{\alpha\text{-brass}}//(220)_{Pb}$ interface with $[011]_{\alpha\text{-brass}}//[\bar{1}13]_{Pb}$ orientation were simulated by molecular dynamics using a sandwiched cell (shown in Fig. 12a) comprising two incoherent interfaces for parallel Cu and Pb slabs of orientations $X_1 = [\bar{2}1\bar{1}]_{cu}$, $Y_1 = [011]_{cu}$, $Z_1 = [11\bar{1}]_{cu}$ and $X_2 = [\bar{3}3\bar{2}]_{Pb}$, $Y_2 = [\bar{1}13]_{Pb}$ and $Z_2 = [110]_{Pb}$ (see Supplementary Material for details). After molecular static relaxation at zero temperature, the interfacial configuration is found to feature a (4×4) rhombic structure on the $(220)_{Pb}$ plane relative to the underlying $(11\bar{1})_{Cu}$ plane as shown in Fig. 12b, which is in good agreement with the experiments[23] and

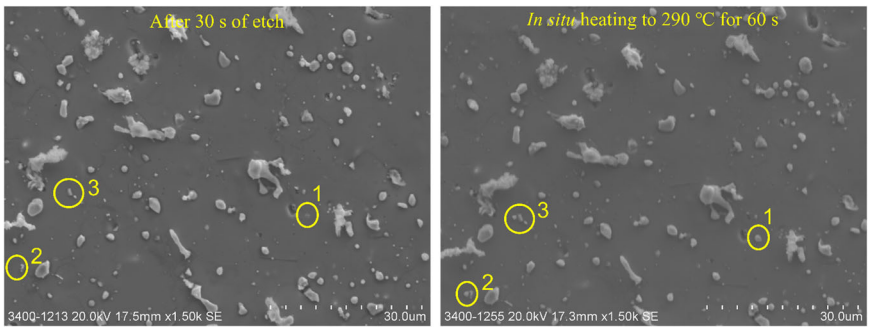

Fig. 9 Surfacing of submicron-sized Pb particles. In situ heating in the SEM at 290 °C for 1 min, of a pw-brass surface preferentially etched by phosphoric acid for 30 s, showing coarsening of Pb particle at 1 and emergence of new Pb particles at 2 and 3.

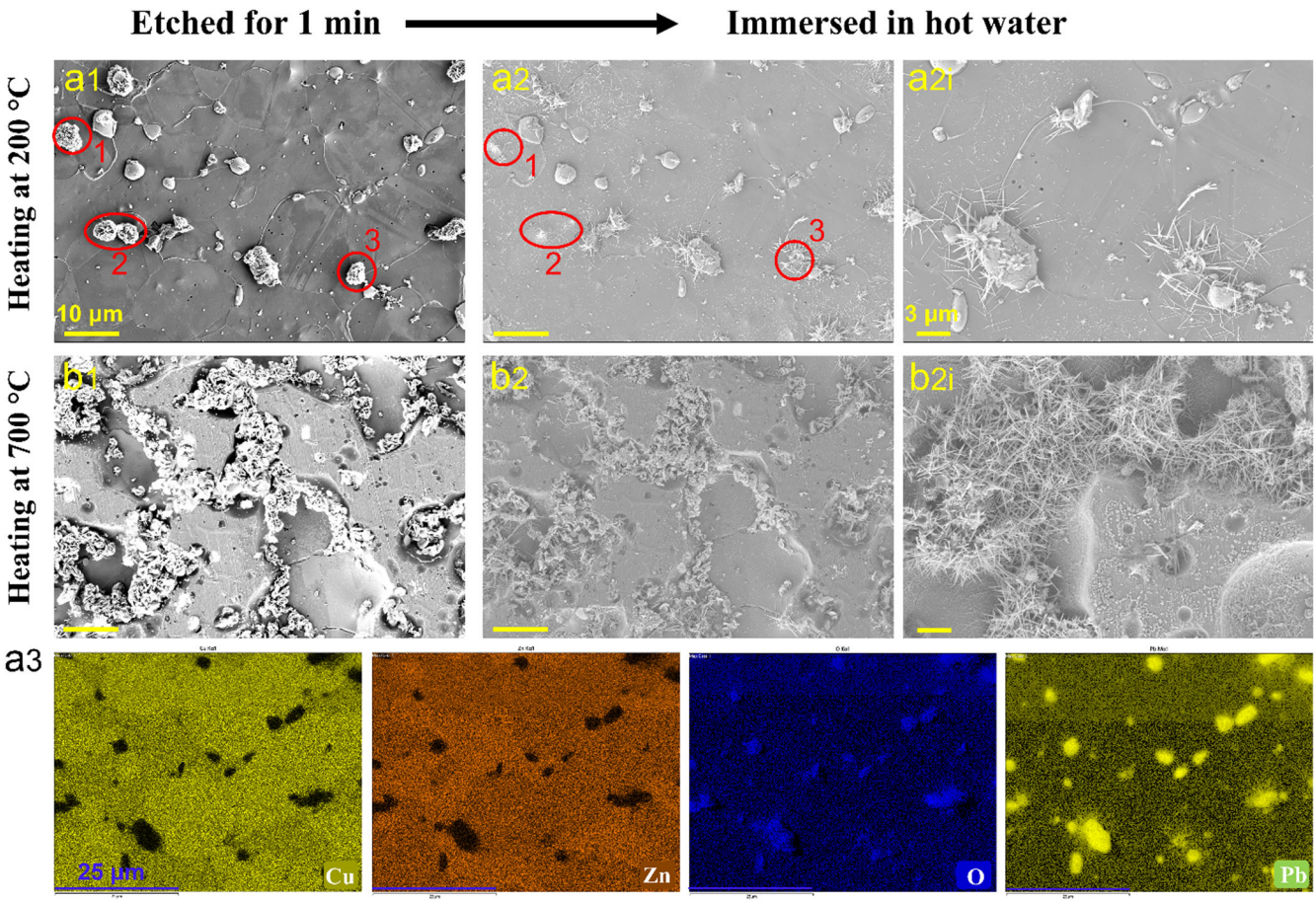

Fig. 10 The morphologies of Pb particles in samples subjected to the two heat treatments exposed by phosphoric-acid etching for 1 min, before and after immersion in hot water at 75 °C. The morphologies of Pb particles (**a1**, **b1**) after heat treatment at 200 and 700 °C, respectively, followed by etching for 1 min in phosphoric acid, **a2**, **b2** after subsequently immersed in hot water at 75 °C for 45 min. **a2i**, **b2i** are enlargements of **a2**, **b2** to show more clearly the fine details of the needles. **a3** shows element maps of the etched sample after ~45 min of hot-water immersion.

simulations[24] on epitaxially deposited Pb on (111) Cu surface below the melting point of Pb. Also, the adhesion energy of $(11\bar{1})_{Cu}//(220)_{Pb}$ is predicted to be positive at 0.889 J m^{-2} (Supplementary Material), indicating that the current $(11\bar{1})_{Cu}//(220)_{Pb}$ interface is strongly cohesive and stable, which helps to rationalize the observation in Fig. 4e.

To understand the diffusion voids (Fig. 8) and surfaced Pb particles (Fig. 9), we note that the diffusion constant of self-diffusion in Pb is known to obey the Arrhenius law[25]

$$D = 0.281 \times \exp(-12183.6/T)\mathrm{cm}^2\,\mathrm{s}^{-1} \quad (1)$$

where T is the absolute temperature. Hence, for heat treatment at 200 °C for 5 min (Fig. 8),$D = 1.829 \times 10^{-16}$ m^2 s^{-1}, and diffusion distance $\sim \sqrt{Dt} = \sqrt{1.829 \times 10^{-16} \times 300} \sim 0.2$ μm.

Such a length scale tallies well with the subsurface depths of the voids seen in Fig. 8a, and the size of the submicron voids seen in Fig. 8b. For the case in Fig. 9 where heat treatment was at 290 °C for 1 min, $D = 1.123 \times 10^{-14}$ m^2 s^{-1}, and diffusion distance $\sim \sqrt{1.123 \times 10^{-14} \times 60} \sim 0.8$ μm, which also tallies well with the size of the newly surfaced particles at sites 2 and 3 in Fig. 9b.

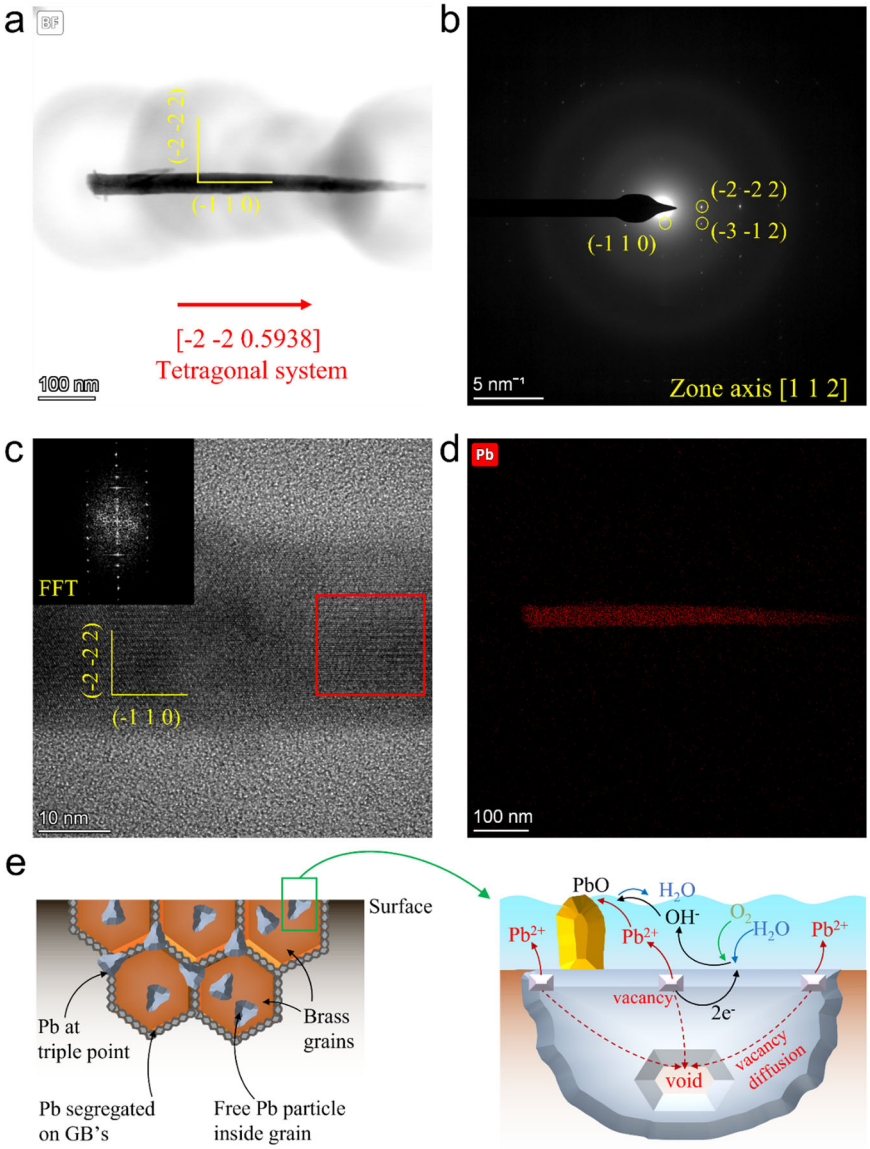

Fig. 11 TEM characterization of PbO needle. a Bright-field image of a needle. **b** Selected area electron diffraction (SAED) pattern used to determine the growth (axial) direction of the needle, namely, [$\bar{2}\bar{2}$0.5938] which is the normal direction of the ($\bar{2}\bar{2}$2) plane in the tetragonal crystal-structure system; **c** HRTEM image of the needle (inset is FFT pattern from the red frame marked). **d** EDS analysis of the needle in (**a**). **e** Proposed mechanism of PbO needle formation by oxidation of surfaced Pb content upon immersion in water.

On heating to 700 °C, the Pb content should have melted and expanded in volume, and hence the formation of the low-sphericity sheets in Fig. 6 is likely a result of the rapid thermal expansion of Pb on melting, which forces the Pb into the $\{101\}_{brass}$ planes which are the least atomically dense planes in the brass structure. To test this conjecture, MD simulation of the thermal expansion of a Pb slab in a Cu matrix was carried out, by using a simulation cell comprising a $\{100\}_{Pb}$ slab of Pb inserted into a Cu simulation cell with orientation $X = [112]_{Cu}$, $Y = [\bar{1}11]_{Cu}$ and $Z = [1\bar{1}0]_{Cu}$ as shown in Fig. 12c. The cell was then heated up to 1000 K at 2 K/ps, and then thermal stress is generated in the Cu phase near the tip of the Pb slab as shown in Fig. 12d. The deviatoric component of the thermal stress fluctuates but generally grows on heating to about 317 K, reaching a value of ~190 MPa. Under such a high shear stress, partial dislocations are seen to emit in the Cu matrix from near the tip of the Pb slab, as shown in Fig. 12e. Due to the successive relaxation events during the heating, the deviatoric stress fluctuates and exhibits a decreasing trend on further heating up to 1000 K. Although the MD simulation here is for the Pb–Cu system and of a very short time scale, the results here do indicate a high magnitude of shear stress developed in the brass matrix of the present pw-grade brass due to the thermal expansion of the Pb particles and the possibility that the brass matrix can plastically deform during heat treatment up to 700 °C to accommodate the expansion of Pb into sheets along the $\{101\}_{brass}$ planes (Fig. 6).

Finally, as shown in Figs. 10 and 11a–d, on immersion in water the surfaced Pb after heat treatment at 200 or 700 °C quickly oxidizes into PbO needles along the normal direction of $\{\bar{2}\bar{2}2\}_{PbO}$ planes. Figure 11e shows the possible formation mechanism of the PbO by oxidation of an exposed Pb particle during contact with water. With oxygen dissolved into the water, the following reactions may occur:

$$\text{At anode}: Pb \rightarrow Pb^{2+} + 2e^{-} \quad (2)$$

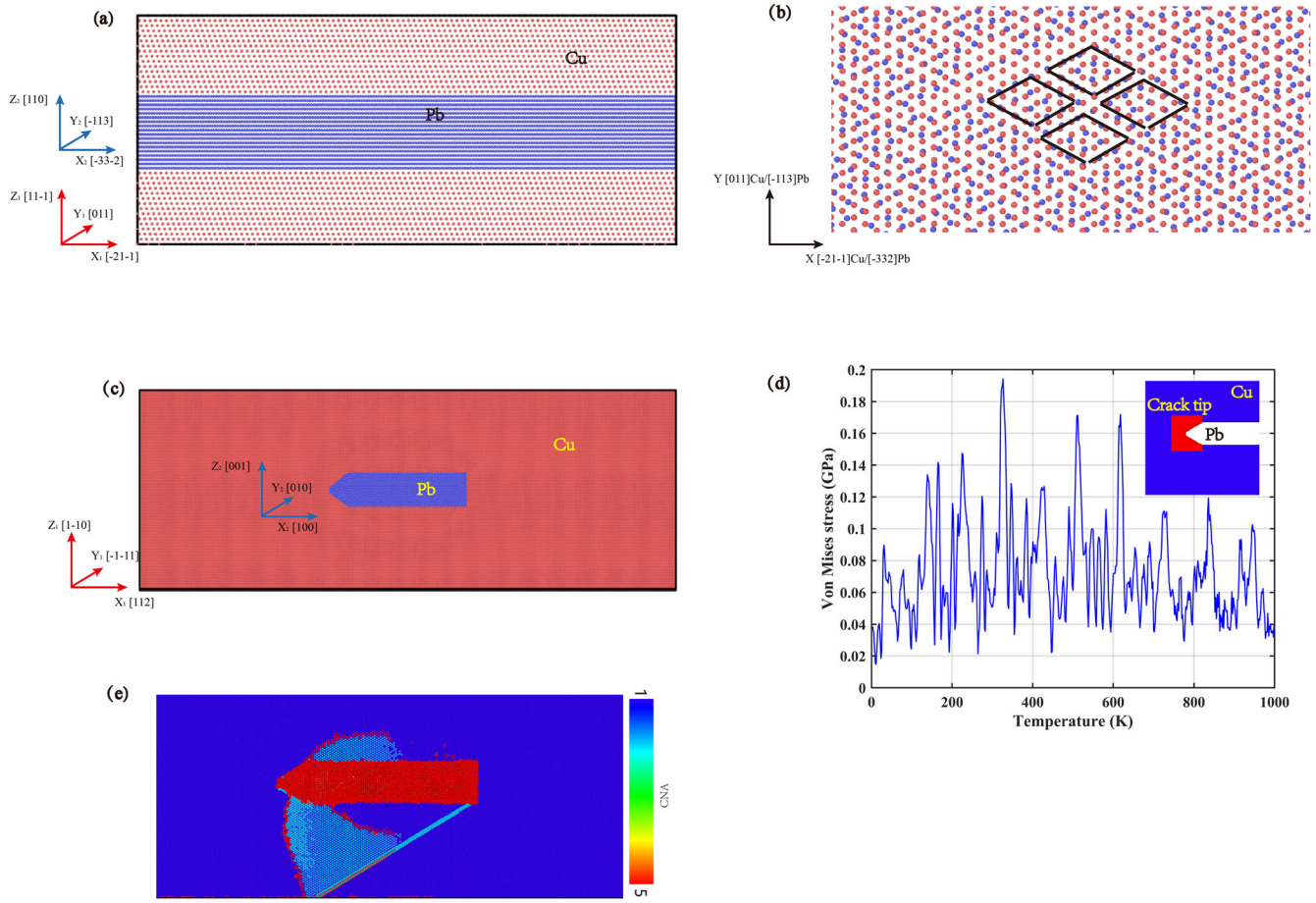

Fig. 12 Molecular dynamics simulations (see Supplementary Material for details). a Schematic representation of a Cu–Pb sandwich slab. **b** Snapshot of the Cu$(11\bar{1})_{\alpha}$//Pb(220) interface morphology, Cu and Pb are red and blue atoms, respectively. **c** Schematic representation of a Pb sheet inserted inside a Cu block. **d** Deviatoric (von Mises) stress developed in the Cu matrix in the red zone near the tip of the Pb slab, vs. the simulation temperature. **e** Partial dislocations emitted in the Cu matrix when heating the Cu–Pb block to 317 K, CNA = 1, 2 for FCC and HCP lattice, respectively.

At the cathode (in a slightly alkaline medium pertinent to the usual drinking water condition):

$$H_2O + 1/2O_2 + 2e^- \rightarrow 2OH^- \quad (3)$$

$$\text{PbO formation}: Pb^{2+} + 2OH^- \rightarrow PbO + H_2O \quad (4)$$

The overall oxidation reaction is $Pb + ½\ O_2 \rightarrow PbO$, but the above anodic and cathodic reactions will have to occur at the corresponding sites shown in Fig. 11e.

The above-identified pathways for Pb diffusion, surfacing and leaching in/from pw-brass are interesting consequences of the immiscibility of the Pb and brass phases[21]—the insoluble Pb exists as a free phase within the brass matrix (Fig. 2), at grain boundaries (Fig. 2) and at their triple points (Figs. 2 and 4a), and upon heating and/or melting, it quickly expands and forces its way along grain boundaries or even into the matrix of the surrounding brass forming interpenetrating lattices (Fig. 4e) or sheets (Figs. 5 and 6). While this leads to the undesirable consequence of easy surfacing and leaching, it is exactly the same immiscible property that leads to the good machinability of the material, namely, mechanical deformation also enhances the surfacing of Pb[19] which would act as a lubricant to ease machining[20]. Easy machinability and leaching of pw-brass are therefore due to a common root and it is unfortunately the former that makes the material so attractive and difficult to replace based on commercial considerations. The immiscibility property also makes the free Pb contents adopt highly illusive physical forms and diffusion/surfacing pathways in brass, which are strongly affected by the polycrystalline structure of the brass matrix, the shape and size of the specimen, and how the material is made or thermo-mechanically treated in the first place. As mentioned before this poses great challenges in designing a quantitative analysis on how leaching is affected by external factors, as finding microstructurally similar samples to check measurement repeatability would be very difficult. Nevertheless, this work has identified the metallurgical pathways for Pb leaching, which should form a solid scientific basis for further mechanistic understanding of how thermal treatment would affect leaching. The results here should also be useful for the design of mitigating measures against Pb leaching from pw-brass, given that this material is unlikely to be banned in the foreseeable future.

In this work, the following aspects of Pb leaching from pw-brass have been discovered:

1. Pb microstructures in pw-brass after heat treatment at 200 and 700 °C pertinent to soldering and brazing joining of pipe components. At 200 °C, Pb existing in isolated or connected particles (especially at grain-boundary triple points) of high sphericity rapidly diffuses into the surrounding brass matrix, forming an interpenetrating lattice structure with a $[011]_{\alpha\text{-brass}}//[\bar{1}13]_{Pb}$, $(11\bar{1})_{\alpha\text{-brass}}//(220)_{Pb}$ orientation relationship, as one identified pathway. At 700 °C, Pb originally in isolated or connected particle forms

melts and expands in volume, thus forcing itself into the brass lattice preferentially along $\{101\}_{\alpha\text{-brass}}$ planes, forming Pb phase of low sphericity or even large sheets.
2. At 200 °C and above, the surfacing of Pb contents happens rapidly over durations of minutes by diffusion. Voids are left behind in the brass matrix after Pb surfacing.
3. At low immersion temperatures in water, the surfaced Pb oxides into needle-shaped PbO along the direction normal to the $\{\overline{2}\overline{2}2\}$ planes of the tetragonal crystal structure. For heating times longer than 20 min, 700 °C pre-treated pw-brass has significantly more PbO formed than 200 °C pre-treated pw-brass, presumably due to the formation of the large Pb sheets that would allow more continuous supply of Pb to the surface during prolonged water immersion.

These findings contribute to a thorough mechanistic understanding of how leaching occurs in potable-water-grade brass and will assist in the design of mitigating measures for Pb leaching.

METHODS

Materials processing

To better represent the realistic market supply of pw-brass products, the experimental materials used in this study were brass fittings of ecFIT model 401C ×C Elbow with 22 mm diameter. This product is qualified for the General Acceptance (GA) scheme (GA number 20190470) issued by the Water Supplies Department (WSD) for use in freshwater services in Hong Kong[26]. The test report on elemental composition with Spark OES on brass samples was issued by Furgo Technical Services Limited, a certified laboratory in the Hong Kong Laboratory Accreditation Scheme (HOKLAS), as a supporting document for the qualification of the said brass product. To standardize the shape of the brass products used in this study, the purchased samples were cut into cylindrical shells with 22 mm inner diameter, 1.5 mm wall thickness, and 20 mm height for heating in a furnace, and $10 \times 10 \times 1$ mm for scanning electron microscopy (SEM). The solution used for electrochemical etching of brass surfaces was 25% phosphoric acid + 25% ethanol absolute + 50% deionized water. The test water was prepared in compliance with AS/NZS 4020: 2018 'Testing of products for use in contact with drinking water—Appendix H: Test Methods—Metals'[27]. Water samples after the immersion tests were then sent to the Hong Kong Standards and Testing Centre (STC) for lead concentration measurement using inductively coupled plasma-mass spectroscopy (ICP-MS). All data acquisition was performed using the Thermo Fisher iCAP RQ model, which has a detection limit at the part-per-billion (ppb) level for Pb. For each heating temperature, four samples were tested for Pb leaching to obtain statistical variance in the result.

Characterization techniques

Conventional electron microscopy. The surface morphologies of pw-brass were characterized by a Leo 1530 FEG scanning electron microscope (SEM). Crystal orientations were characterized by using an SEM equipped with an electron backscatter diffraction (EBSD) system (Oxford Instruments NordlysNano EBSD Detector with AZtecHKL). For the TEM study of Pb particles, the specimens were prepared through mechanical polishing and ion milling for the TEM (Thermo Scientific Talos F200X STEM) observation. The chemical compositions of the brass products were measured by inductively coupled plasma optical emission spectroscopy (ICP-OES, PerkinElmer Avio 200) as: 58.88%Cu, 36.56%Zn, 0.51%Fe, 0.35%Ni, 0.29%Pb by weight. X-ray diffractometry (XRD, Brucker D8 Advance) identified the lattice structure of the brass as α-brass with face-centered cubic (FCC) crystal structure (Supplementary Material Fig. 4). Using a conventional lift-out technique, needle specimens for nanoscale X-ray 3D imaging experiment were prepared by gallium focused-ion-beam (FIB) milling on a FIB-SEM dual-beam system (Helios NanoLab600i, FEI). Surface cutting of the heated samples and microstructural observation underneath the surface was performed in an FEI Quanta 200 3D FIB microscope.

Synchrotron radiation X-ray imaging. To characterize the spatial distribution of Pb in the pw-brass, a nanoscale X-ray CT experiment was performed on the 4W1A beamline at the Beijing Synchrotron Radiation Facility (BSRF)[28]. The high-resolution-imaging-field-of-view mode was adopted with a field-of-view size of 15 μm × 15 μm, a resolution of 50 nm, an energy of 8 keV, and an exposure time of 20 s. Three-dimensional reconstruction and visualization were performed using the Avizo software package.

In-situ heating SEM observation. Pw-brass sample surfaces were polished with silicon-carbide sandpapers on a Buehler EcoMet™ Manual Single Grinder Polisher down to different fineness, with grit 240 being the roughest and grit 4000 the finest. For SEM observation, indentation markers were made on the specimen surface by a Buehler Micromat 2100 hardness tester equipped with a Vickers diamond indenter tip and an indenter load of 0.05 kg, for clearer observation and tracking. The imaging was conducted by heating the brass samples at 50 °C increments from room temperature to 200 °C, followed by 25 °C increments between 200 and 300 °C, and holding each temperature for 5 minutes inside a Hitachi S-3400N SEM in a vacuum state, followed by a decrease in temperature to 200 °C for 5 min. Afterward, the Pb content was measured using energy-dispersive X-ray analysis (EDX) in the SEM; however, it should be noted that the EDX function could not be used simultaneously with heating.

DATA AVAILABILITY

The relevant data are available from the corresponding authors upon reasonable request.

CODE AVAILABILITY

Codes are available upon request to the corresponding author.

Received: 26 April 2023; Accepted: 5 August 2023;
Published online: 14 August 2023

REFERENCES

1. Violante, A., Cozzolino, V., Perelomov, L., Caporale, A. G. & Pigna, M. Mobility and bioavailability of heavy metals and metalloids in soil environments. *J. Soil Sci. Plant Nutr.* **10**, 268–292 (2010).
2. Stathatou, P. M. et al. Lead removal at trace concentrations from water by inactive yeast cells. *Commun. Earth Environ.* **3**, 132 (2022).
3. Sun, G. L., Reynolds, E. E. & Belcher, A. M. Using yeast to sustainably remediate and extract heavy metals from waste waters. *Nat. Sustain.* **3**, 303–311 (2020).
4. Santucci, R. J. & Scully, J. R. The pervasive threat of lead (Pb) in drinking water: unmasking and pursuing scientific factors that govern lead release. *Proc. Natl Acad. Sci. USA* **117**, 23211–23218 (2020).
5. Edwards, M. Fetal death and reduced birth rates associated with exposure to lead-contaminated drinking water. *Environ. Sci. Technol.* **48**, 739–746 (2014).
6. Canfield, R. L. et al. Intellectual impairment in children with blood lead concentrations below 10 microg per deciliter. *N. Engl. J. Med.* **348**, 1517–1526 (2003).
7. BS EN 1057:2006 + A1, 2010. Copper and copper alloys. *Seamless, Round Copper Tubes for Water and Gas in Sanitary and Heating Applications*. British Standard.
8. Tang, M., Sinsheimer, P., Sarver, E., Parks, J. & Edwards, M. Evaluating "Lead-Free" brass performance in potable water. *Corrosion* **75**, 865–875 (2019).
9. Environmental Protection Agency. The US Government Lead-Free Definition, Safe Drinking Water Act. https://www.epa.gov/sdwa (2014).
10. Harvey, P. J., Handley, H. K. & Taylor, M. P. Widespread copper and lead contamination of household drinking water, New South Wales, Australia. *Environ. Res.* **151**, 275–285 (2016).

11. Roy, S., Tang, M. & Edwards, M. A. Lead release to potable water during the Flint, Michigan water crisis as revealed by routine biosolids monitoring data. *Water Res.* **160**, 475–483 (2019).
12. Renner, R. Out of plumb when water treatment causes lead contamination. *Environ. Health Perspect.* **117**, A542–A547 (2009).
13. Deshommes, E., Prevost, M., Levallois, P., Lemieux, F. & Nour, S. Application of lead monitoring results to predict 0–7 year old children's exposure at the tap. *Water Res.* **47**, 2409–2420 (2013).
14. Deshommes, E., Laroche, L., Nour, S., Cartier, C. & Prevost, M. Source and occurrence of particulate lead in tap water. *Water Res.* **44**, 3734–3744 (2010).
15. Riblet, C., Deshommes, E., Laroche, L. & Prevost, M. True exposure to lead at the tap: insights from proportional sampling, regulated sampling and water use monitoring. *Water Res.* **156**, 327–336 (2019).
16. Dore, E., Deshommes, E., Laroche, L., Nour, S. & Prevost, M. Lead and copper release from full and partially replaced harvested lead service lines: impact of stagnation time prior to sampling and water quality. *Water Res.* **150**, 380–391 (2019).
17. Dore, E., Deshommes, E., Andrews, R. C., Nour, S. & Prevost, M. Sampling in schools and large institutional buildings: Implications for regulations, exposure and management of lead and copper. *Water Res.* **140**, 110–122 (2018).
18. Pieper, K. J. et al. Evaluating water lead levels during the Flint water crisis. *Environ. Sci. Technol.* **52**, 8124–8132 (2018).
19. Siu, K. W., Kwok, J. C. M. & Ngan, A. H. W. Thermo-mechanical processing of brass components for potable-water usage increases risks of Pb leaching. *Water Res.* **186**, 116414 (2020).
20. Stoddart, C. T. H., Lea, C., Dench, W. A., Green, P. & Pettit, H. R. Relationship between lead content of Cu–40 Zn, machinability, and swarf surface composition determined by Auger electron spectroscopy. *Metals Technol.* **6**, 176–184 (1979).
21. Kawazoe, Y. et al. *Phase Diagram Cu–Pb–Zn* (Springer Materials, 1997).
22. Bartoňová, L., Raclavská, H., Čech, B. & Kucbel, M. Behavior of Pb during coal combustion: an overview. *Sustainability* **11**, 6061 (2019).
23. Müller, S., Prieto, J. E., Rath, C. & Hammer, L. Surfactant-induced surface restructuring: (4 × 4)-Pb/Cu (111). *J. Phys.: Condens. Matter* **13**, 1793 (2001).
24. Vamvakopoulos, E., Papageorgiou, D. G. & Evangelakis, G. A. Solidification of Pb overlayer on Cu(111) surface by molecular dynamics simulation. *Thin Solid Films* **485**, 290–295 (2005).
25. Nachtrieb, N. H. & Handler, G. S. Self-diffusion in lead. *J. Chem. Phys.* **23**, 1569 (1955).
26. Surveillance Programme for the General Acceptance System, WSD Circular Letter No. 8 (2017). https://www.wsd.gov.hk/en/plumbing-engineering/pipes-and-fittings-to-be-used-in-inside-service-or/surveillance-programme-for-ga-system-/.
27. Standards Australia, SAI Global. *Testing of Products for use in Contact with Drinking Water, Appendix H: Test Methods—Metals, AS/NZS: 4020* (Standards Australia, SAI Global, 2018).
28. Zhang, C. et al. Multifunctional nanoprobe for 3D nanoresolution imaging of intact cell HER2 protein with hard X-ray tomography. *Anal. Chem.* **95**, 2129–2133 (2023).

ACKNOWLEDGEMENTS

This work was supported by the Research Impact Fund of the Research Grants Council, Hong Kong SAR Government (project code: RIF R7012-20). WanXia Huang, Kai Zhang, QingXi Yuan, Xing Zhong Cao, Baoyi Wang, Xiao Liu, ShanFeng Wang, and ChunXia Yao are acknowledged for their help on the synchrotron radiation X-ray imaging experiments which were performed at the 4W1A beamline of the Beijing Synchrotron Radiation Facility (BSRF), Beijing, China.

AUTHOR CONTRIBUTIONS

The study was conceived by T.Z. and A.H.W.N. and supervised by A.H.W.N. T.Z. and L.Y. performed the synchrotron radiation X-ray imaging experiments and analysis of the XCT data. W.L. performed the MD simulations. J.C.M.K. conducted the leaching tests on water samples. T.Z., K.W.S., L.Y., and J.C.M.K. conducted the SEM/TEM. The paper was drafted by A.H.W.N., T.Z., and W.L., finalized by A.H.W.N., and agreed upon by all authors.

COMPETING INTERESTS

The authors declare no competing interests.

ADDITIONAL INFORMATION

Supplementary information The online version contains supplementary material available at https://doi.org/10.1038/s41529-023-00389-8.

Correspondence and requests for materials should be addressed to Alfonso Hing Wan Ngan.

Reprints and permission information is available at http://www.nature.com/reprints

Publisher's note Springer Nature remains neutral with regard to jurisdictional claims in published maps and institutional affiliations.